②

REPORT DOCUMENTATION PAGE		READ INSTRUCTIONS BEFORE COMPLETING FORM
1. REPORT NUMBER 16436.5-EL	2. GOVT ACCESSION NO. N/A A127 238	3. RECIPIENT'S CATALOG NUMBER N/A
4. TITLE (and Subtitle) Prediction of Transverse-Mode Selection in Double Heterojunction Lasers by an Ambipolar Excess Carrier Diffusion Solution		5. TYPE OF REPORT & PERIOD COVERED Reprint
		6. PERFORMING ORG. REPORT NUMBER N/A
7. AUTHOR(s) Joseph B. Delaney Richard R. Shurtz, II Jerome K. Butler		8. CONTRACT OR GRANT NUMBER(s) DAAG29 80 K 0004
9. PERFORMING ORGANIZATION NAME AND ADDRESS Southern Methodist University Dallas, TX 75275		10. PROGRAM ELEMENT, PROJECT, TASK AREA & WORK UNIT NUMBERS N/A
11. CONTROLLING OFFICE NAME AND ADDRESS U. S. Army Research Office P. O. Box 12211 Research Triangle Park, NC 27709		12. REPORT DATE Feb 83
		13. NUMBER OF PAGES 10
14. MONITORING AGENCY NAME & ADDRESS(if different from Controlling Office)		15. SECURITY CLASS. (of this report) Unclassified
		15a. DECLASSIFICATION/DOWNGRADING SCHEDULE

16. DISTRIBUTION STATEMENT (of this Report)

Submitted for announcement only.

DTIC
ELECTE
APR 2 1 1983
B

17. DISTRIBUTION STATEMENT (of the abstract entered in Block 20, if different from Report)

18. SUPPLEMENTARY NOTES

19. KEY WORDS (Continue on reverse side if necessary and identify by block number)

20. ABSTRACT (Continue on reverse side if necessary and identify by block number)

83 04 21 037

Prediction of transverse-mode selection in double heterojunction lasers by an ambipolar excess carrier diffusion solution

Joseph B. Delaney

TRW, Optoelectronics Division, Carrollton, Texas 75006

Richard R. Shurtz, II

Night Vision and Electro-optics Laboratory, Laser Division, Fort Belvoir, Virginia 22060

Jerome K. Butler

Southern Methodist University, Dallas, Texas 75275

Transverse-mode selection is characterized for GaAs/AlGaAs double heterojunction lasers from optical field and electron/hole interaction. The electron/hole distribution determined from a solution of the ambipolar diffusion equation provides the necessary information about gain/mode coupling to predict the current at threshold. Lasing power out versus current solutions provide information about internal differential quantum efficiency. Theory is matched to experiment for a multimode laser with one heterojunction having a very small index step. It is found that the laser's characteristics over a temperature and current range are predicted by adjusting the active-layer refractive index as determined from far-field measurements.

PACS numbers: 42.55.Px, 42.60.By

I. INTRODUCTION

In recent years, there has been considerable effort spent fabricating various semiconductor laser-device geometries for control of mode operation. In GaAs/AlGaAs devices, the transverse-mode operation is usually governed by the growth of various layer thicknesses and index steps at the grown heterojunctions. Double heterojunction lasers which confine the optical field to the thin active layers usually operate in the fundamental mode. Furthermore, the lasing mode is independent of drive because small index changes due to injection have negligible effects on mode selection. While transverse-mode lasing can be well controlled by epitaxial heterojunctions, lateral-mode operation in contemporary lasers is drive sensitive. Stripe-contact devices[1-3] have lateral guides defined only by the current density which affects the gain distribution while more sophisticated structures[4-7] have grown layers whose thicknesses are functions of lateral positions. Thus, in these devices the lateral modes are shaped by the lateral effective index as well as gain variations.

Because the gain distribution plays a major role in defining mode stability in lasers, it is important to understand the mechanisms of electron/hole transport in active layers. In this paper, we discuss the transverse-mode operation of lasers which are affected by the electron/hole distribution. For the first time the ambipolar diffusion equation is solved for the active layer in an injection laser. The direct consequence of this solution is the ability to predict crossover of competing modes in the active layer. In contrast to ambipolar diffusion, assuming simple electron injection does not explain this phenomena in sufficient detail.

In this work we investigate mode selection from the standpoint of the exact selection process. This includes mode gain coupling and differential quantum efficiency. We concentrate on the transverse (perpendicular to the junction plane) modes in a double heterojunction laser. The excess carrier distribution is assumed ambipolar and a complete solution is obtained. From mode/gain coupling, it is possible to predict the threshold, and from the slope efficiency, it is possible to predict mode crossover.

The laser we apply this to is a broad-area double heterojunction GaAs device with a small index step at one of the heterojunctions. The laser is heated over a temperature range and the first two modes are investigated. It is found that cavity-mode preference is very sensitive to temperature and current level. Application of the diffusion equation is used to describe the crossover of the first two modes and it is established that the mode with the highest slope efficiency will dominate. Far-field patterns are described by standard multilayer waveguide techniques. Finally, a calculation is made to estimate the effect of free carriers on the refractive index in the material.

II. THEORY
A. Approach

Excess carrier movement in the active layer of an injection laser is described using the ambipolar diffusion equation. Quasi-Fermi level continuity as well as electron and hole current continuity is imposed at each interface. The quasi-Fermi level location is calculated using a nonparabolic Γ_{1C} extremum, and parabolic X_{1C} and Γ_{15V} extrema. The boundary condition is set up in such a way as to eliminate the need for a solution within the space charge layer surrounding each interface. The spontaneous recombination lifetime is calculated without imposing quasimomentum conservation for parabolic bands. Above threshold, a stimulated recombination term is included in the ambipolar diffusion equation and the gain is assumed to be pinned at the threshold value. The lasing modal shape for the transverse modes (perpendicular to the metallurgical junctions) is calculated by solving Maxwell's equations for a multilayer dielectric wave guide.

B. The excess carrier distribution

The diffusion equation evolves along the standard route. We demand, as is customary, that each carrier type

satisfies the continuity equation[8]

$$D_p \nabla^2 p - \mu_p \nabla \cdot (p\overline{E}) + g_p - p/\tau_p = \partial p/\partial t, \quad (1a)$$

$$D_n \nabla^2 n + \mu_n \nabla \cdot (n\overline{E}) + g_n - n/\tau_n = \partial n/\partial t, \quad (1b)$$

where n, p = total electron, hole carrier density; D_n, D_p = electron, hole diffusion constant; g_n, g_p = electron, hole generation rate; and τ_n, τ_p = electron, hole mean recombination time. We further demand that Poisson's equation be satisfied:

$$\nabla \cdot \overline{E} = (4\pi\rho/\epsilon), \quad (2)$$

where ρ is the space charge density and ϵ is the dielectric constant.

Rather than solve Eqs. (1) and (2) exactly, we take an approximate route where we assume that the internal field between the electron and hole charge densities is strong enough to guarantee charge neutrality. Although this condition is violated in the space charge layer surrounding the heterojunctions, we can formulate the problem in such a way that only diffusion processes outside the heterojunctions need be considered. Under this assumption, the excess electron and hole densities, δn and δp, respectively, must be equal:

$$\delta n = n - n_0 = p - p_0 = \delta p. \quad (3)$$

Here, n_0, p_0 designate the thermal-equilibrium carrier densities. If we take $(\partial n_0)/(\partial x) - (\partial p_0)/(\partial x) = 0$, we can substitute Eq. (3) into Eq. (1) to obtain two equations for the two unknowns δp and $\overline{E}$. The terms involving $\nabla \cdot \overline{E}$ can be eliminated by multiplying Eq. (1a) by $n\mu_n$ and Eq. (1b) by $p\mu_p$ and adding to obtain[9]

$$D^* \nabla^2 (\delta p) - \mu^* \overline{E} \cdot \nabla (\delta p) + g' - \frac{\delta p}{\tau} = \frac{\partial (\delta p)}{\partial t}, \quad (4)$$

where

δp = excess carrier density,

$$D^* = \frac{n\mu_n D_n + p\mu_p D_p}{n\mu_n + p\mu_p},$$

$$\mu^* = \frac{\mu_n \mu_p (n_0 - p_0)}{n\mu_n + p\mu_p}, \quad g' = g'_n = g'_p,$$

$$\frac{\delta p}{\tau} = \frac{p_0 + \delta_p}{\tau_p} - \frac{p_0}{\tau_{p_0}} = \frac{n_0 + \delta n}{\tau_n} - \frac{n_0}{\tau_{n_0}},$$

g'_n, g'_p = excess carrier generation rates, and

τ = excess carrier recombination lifetime.

We have implicitly assumed that the net recombination rate $(\delta p)/\tau$ is the same for electrons as for holes, as it must be. We have further assumed that the equilibrium generation rate is equal to the equilibrium recombination rate for both electrons and holes.

For the ambipolar diffusion Eq. (4), observe that the ambipolar diffusion rate for excess carriers is determined by the average value of D_n and D_p, weighted by $n\mu_n$ and $p\mu_p$. In other words, the two oppositely charged clouds interact with each other through the internal field in such a way as to satisfy Poisson's equation and must then diffuse at a naturally acceptable rate. This is crucial because of the very large injected charge densities encountered in injection lasers

$(\sim 2 \times 10^{18} \text{ cm}^{-3})$.

The electric field in Eq. (4) refers to both the internal and applied fields. Under the conditions encountered in an injection laser, these fields exert only a small direct influence on carrier distribution, and as such can be ignored in Eq. (4). In other words, the electric field does not alter the actual excess carrier spatial distribution, but rather only causes carriers to drift. This is the case if the drift length is much less than the diffusion length, i.e.,

$$\mu^* E\tau \ll (D^*\tau)^{1/2}. \quad (5)$$

This condition is met in the solutions ultimately obtained. The major effect of the internal field, that of charge neutrality, is still accounted.

If we assume the only excess carrier drain, other than spontaneous recombination $\delta p/\tau$, is stimulated recombination, then for an infinitely long cavity and time-averaged values[10]

$$r = \frac{\partial (\delta p)}{\partial t} = \frac{1}{\eta_s} \frac{gP(x)}{h\nu}, \quad (6)$$

where $P(x)$ = time-averaged power density, g = gain, η_s = stimulated quantum efficiency, and $h\nu$ = photon energy. For 100% carrier confinement, η_s is the internal differential quantum efficiency. In these calculations we put $\eta_s = 1$. Equation (4) becomes

$$D^* \nabla^2 (\delta p) - (\delta p)/\tau = r, \quad (7)$$

where D^* = ambipolar diffusion constant, τ = spontaneous recombination lifetime, and r = stimulated recombination rate. The value r is equated to zero in the region where $g < 0$. The spontaneous recombination lifetime is

$$\tau = 1/[B(n_0 + p_0 + \delta p)], \quad (8)$$

where B is $1.3 \times 10^{-10} \text{ cm}^3/\text{sec}$.[11,12]

C. The boundary conditions

At each boundary within the device there exists a space charge layer with a width severely reduced under conditions of forward bias. Because quasicharge neutrality is violated within this layer, we match across the layer under the assumptions it is is thin enough and internal fields are strong enough that carriers are swept through without significant recombination. Hence, we demand that the electron and hole current densities be the same on each side of the space charge layer. These densities are written

$$\overline{J}_n = qn\mu_n \overline{E} + qD_n \nabla(\delta p), \quad (9a)$$

$$\overline{J}_p = qp\mu_p \overline{E} - qD_p \nabla(\delta p). \quad (9b)$$

Here, $\overline{E}$ is the total field and q is the electron charge. Although $\overline{E}$ can be ignored in Eq. (7), where it has a small effect, it must be included in the boundary conditions because both drift and diffusion terms are significant.

In addition to continuity of current densities, we also impose continuity of hole and electron quasi-Fermi levels across each layer interface. Although it is clear this alignment of Fermi levels implies band bending, i.e., space charge, we assume an abrupt heterojunction and ignore such effects.

D. The electromagnetic field distribution

The standard multilayer slab dielectric waveguide model is used to describe the transverse far-field patterns.[13,14] Standard calculations yield propagation constants $\gamma = \alpha + j\beta$ and fields. For instance, for a TE mode, we can express the mth-mode field distribution for the ith layer as

$$E'_m(x) = E_m \cos(h'_m x + \phi'_m),\qquad (10)$$

where h'_m is the complex eigenvalue and x is the coordinate across the active region. The overall field solution is obtained by matching the field components at each interface. The far-field pattern then becomes proportional to the Fourier transform of the near field on a lasing facet.

E. The diffusion-equation solution

Assume a three-layer device with the central layer active (see Fig. 3). Also, assume the mode is propagating down the z axis with x perpendicular to the guide. The excess carrier diffusion equations for this case become

$$\frac{d^2(\delta p)}{dx^2} - \frac{\delta p}{(L_i^*)^2} = 0, \quad i = 1,3, \qquad (11a)$$

$$\frac{d^2(\delta p)}{dx^2} - \frac{\delta p}{(L_i^*)^2} = \frac{g(x)P_m(x)}{\eta_s h\nu}, \quad i = 2, \qquad (11b)$$

where $L_i^* = (D^{*'}\tau')^{1/2}$, $g(x)$ is the localized gain and $P_m(x)$ is the optical Poynting vector component along the propagation direction.

These equations are linearized by replacing $g(x)$ with its weighted average within the active region[10]

$$g = \frac{\int_{-\infty}^{\infty} g(x)E_m^2(x)\,dx}{\int E_m^2(x)\,dx} = \frac{g_m N_m}{T_m}, \qquad (12)$$

where N_m is the field normalization constant and T_m is the mode intensity integrated over the active layer. It should be noted that $g(x) = 0$ outside the active region. Further, assuming no losses in layers external to the active region, g_m represents the propagation gain of the mth mode. With D^* and τ assumed to be piecewise constant layer-to-layer, Eq. (11b) becomes

$$\frac{d^2(\delta p)}{dx^2} - \frac{\delta p}{(L_2^*)^2} = \beta_m \cos^2(h_m^2 x + \phi_m^2), \qquad (13)$$

where

$$\beta_m = \frac{g_m P_m E_m^2}{D^* T_m h\nu\eta_s},$$

$$P_m = \int_{-\infty}^{\infty} P_m(x)\,dx.$$

Ignoring the minor effect of the layer 3-4 interface on the carrier distribution, the solution to the diffusion equation in the various layers becomes

$$\delta p_3(x) = G_3 \cosh(x/L_3^*) + F_3 \sinh(x/L_3^*), \qquad (14a)$$

$$\delta p_2 = G_2 \cosh(x/L_2^*) + F_2 \sinh(x/L_2^*)$$
$$\quad - \beta_m (L_2^*)^2/2\left(1 + \frac{\cos^2(h_m^2 x + \phi_m^2)}{1 + (2h_m^2 L_2^*)^2}\right), \qquad (14b)$$

$$\delta p_1(x) = G_1 \cosh(x/L_1^*) + F_1 \sinh(x/L_1^*). \qquad (14c)$$

With these eigenfunctions, the solution follows directly from matching the current density and quasi-Fermi levels at each interface. The Fermi-level continuity condition is applied using Kane's nonparabolicity for the Γ_{1c} minimum and a parabolic expression for both Γ_{15v} and the X_{1c} minima. The effect of aluminum concentration on carrier mobility, effective mass, and band gap is included. The volume recombination rate is related to the optical gain of the laser in linear fashion using coefficients obtained by integrating over parabolic bands without quasimomentum conservation. The recombination lifetime is found in a similar manner. The diffusion coefficients are calculated using the generalized Einstein equation. The complete formulation of the problem is presented elsewhere.[15] The necessary roots are calculated on a computer using a real-root searching routine. The final solution provides current-voltage curves, power output-current curves, threshold current density of each mode, and finally electron and hole injection efficiencies into the active layer.

F. Validation of numerical results

This theory has been applied to double heterojunction lasers, single heterojunction lasers, and separate electron-optical confinement lasers. Close agreement has been found with experimental values. Two typical results for a double heterojunction laser are shown in Figs. 1 and 2. The first shows threshold current density as the active region thickness is reduced, and the second shows threshold as a function of the aluminum concentration in the passive regions. The slope of Fig. 1 is 5.2 kA/cm^2 μm, a value which compares closely with available data.[16,17]
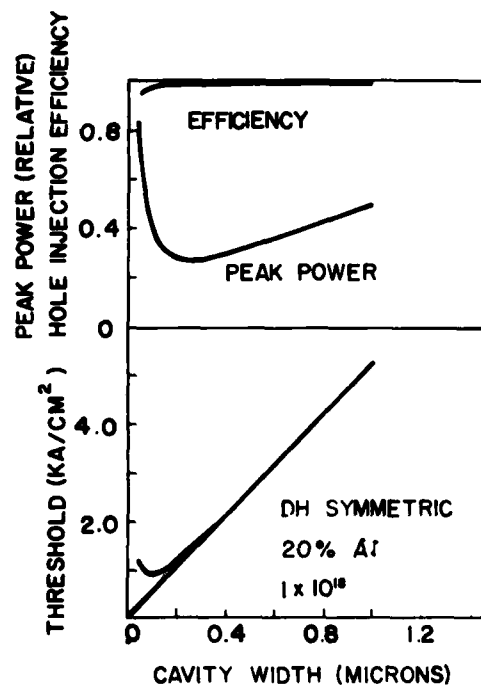

FIG. 1. Calculated hole injection efficiency, relative peak power, and threshold current density of a symmetric DH laser as a function of cavity width. The active layer doping is p-10^{17} cm^{-3} and the passive n-layer doping is 10^{18} cm^{-3}. The passive p layer has a 5×10^{18} cm^{-3} doping level. The AlAs percentage in the outer layers is 20%.
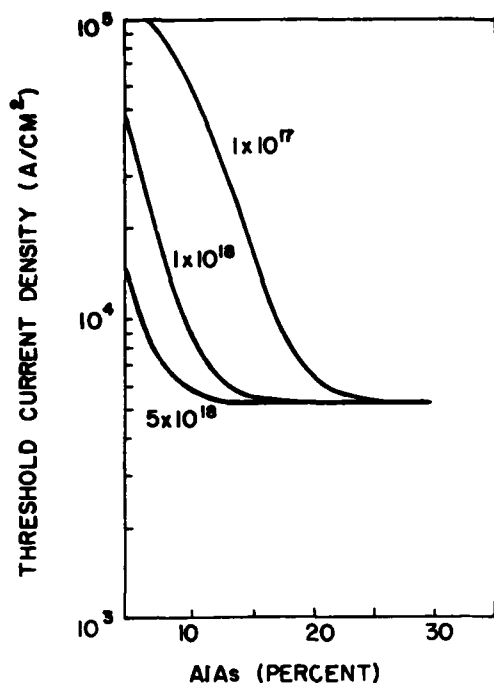
FIG. 2. Calculated threshold current density as a function of AlAs percentage in the GaAlAs passive p layer of a symmetric DH laser with a 1-μm wide GaAs (p-10^{17} cm^{-3}) active layer. Three passive p-layer doping levels are shown. The passive n-layer doping level is 1×10^{18} cm^{-3}.

III. EXPERIMENT

The lasers characterized in this experiment are broad-area double heterojunction lasers grown by liquid phase epitaxy methods. Figure 3 gives the geometry of one such laser, PL174-1-31. Other lasers of this type were characterized, but PL174-1-31 was selected for its transverse modal behavior with temperature due to the small refractive index step at one heterojunction. Estimating the refractive index of the aluminum layers is accomplished using experimental data[18,19] at a lasing wavelength $\lambda = 9000$ Å. This gives $\Delta \eta = 0.62x$, where x is the fraction of aluminum in the solid. The laser has a cross section of 214×356 μm, where the latter is the cavity length. The chip thickness is 77 μm. The
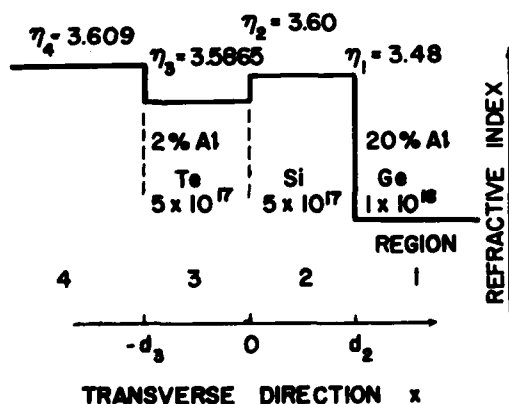
FIG. 3. Geometry of PL174-1-31. For the excess carrier calculation, only layers 1, 2, and 3 are used.

laser is mounted p-side up on the header and has no reflective coating on the facets.

The device is driven with 250-nsec pulses with a 0.01% duty cycle to minimize internal heating. While driven, the laser is heated over temperature range of 20–40 °C. The temperature/current-drive characteristics of the laser are characterized by its far- and near-field dependence.

To measure the far field, the laser is placed on a rotating platter with an axis turned by a 2-rph timing motor. The laser's output is collected by monochromator and amplified by an RCA 7102 photomultiplier tube (PMT). Typical measurement parameters are 2-Å slit width and 750-V bias for the PMT. The output of the PMT is fed to a lock-in amplifier triggered by a reference signal from the pulser. An HP 7560 A log converter and HP 2470 A$\times$10 dc multiplier process the signal for the y axis of a chart recorder. An impedance matching network allows the y axis to be calibrated to three decibels per inch deflection. The calibration is good for over five decades of response. The speed of the x axis, combined with the 2-rph timing motor presents 24° rotation per inch deflection for the x axis. An alternative presentation is to load the PMT with a 50-Ω terminator and display the output pulse on a sampling oscilloscope with a 50-Ω input. This provides a time decomposition of the light-output pulse for ready comparison to the current-input pulse. Patterns were typically made with $J = 1.1J_{\text{th}}$.

The measurement scheme for the near field is accomplished by attaching the laser mount to a micropositioner which has a three-dimensional adjustment. A microscope objective with 160 magnification is mounted opposite the laser facet and a video camera collects the output of the objective lens and displays the image on a monitor.

Peak threshold current values for laser PL174-1-31 are shown in Fig. 4. Triangles denote the fundamental mode whereas crosses mark the second. In the heat-sink temperature range 20–28 °C, only the second mode is present; for 28–42 °C, both fundamental and second modes are present; and above 42 °C, only the fundamental mode propagates. The lasing wavelengths for the two modes are shown in Fig. 5.

The multilayer waveguide model is used to describe the transverse far-field patterns of the modes. Figure 6 is an example of a match of the second mode at 20 °C. The solid curve is the measured pattern, and the dashed curve is the match. The bump on one shoulder at 21.6° of Fig. 6 is the result of light coupling to the lossy substrate. This bump can be accurately positioned to match the experimental pattern by applying Snell's law at the substrate-air interface. The internal angle from the normal to the facet θ' is given by $\tan \theta' \simeq \theta' \simeq h''_4/\beta \simeq \eta_4 \sin \theta$. Here, h''_4 is the imaginary part of h_4, the real propagation constant $\beta = \text{Im}\{\gamma\}$, θ is the external angle to the normal to the facet, and η_4 is the refractive index of the substrate. The relative intensity or amplitude of the bump is adjusted by the separating width d_3.

θ_{pp} is defined as the angle separating the two major lobes of the second mode. The solid line in Fig. 7 shows how θ_{pp} changes over the temperature range. The dashed line in Fig. 7 is the multilayer θ_{pp} versus the active-region refractive index η_2. Over the entire range 20–42 °C the active-region index depression necessary to match experimental evidence
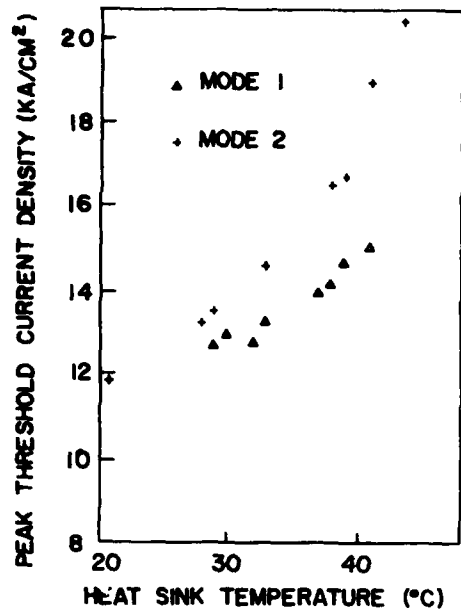
FIG. 4. Peak threshold current vs heat-sink temperature. The triangles are data points for the fundamental mode and the crosses for the second mode of PL174-1-31.
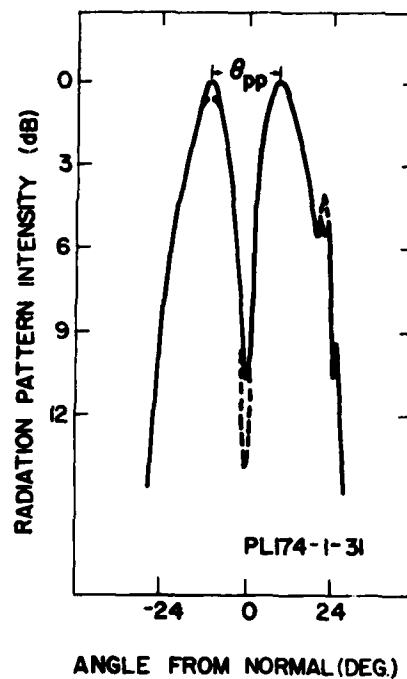

ANGLE FROM NORMAL (DEG.)

FIG. 6. Experimental (solid line) and theoretical (dashed line) far-field patterns for the second mode of PL174-1-31 at 20°.

is $\delta\eta = -0.002$. The fundamental mode also is marked by this refractive index decrease over the temperature range. The half-power full-width of the fundamental transverse mode $\theta_\perp$ decreased over 28–42 °C in a manner consistent with the $\delta\eta$ calculated for the second mode. The second-mode lobe-separation angle θ_{pp} was chosen for calculations for better accuracy.

An interesting feature of this laser is the cavity selection of modes at an intermediate temperature of 38 °C, where Fig. 4 suggests both lower-order modes may exist during a current pulse. In Figs. 8(d) and 8(e) the far field is filtered with the monochromator and the output of the photomultiplier is

fed into the sampling scope with a 50-Ω termination. The top pulse of each picture is the current pulse while the lower is the optical pulse of the laser. It was established during the experiment, from output pulses as in Fig. 8 and from near-field pictures, that the laser switched modes during the current pulse. The discussion to follow explains this multimode switching with current magnitude at an intermediate temperature. Theoretical results accompanying the experiment

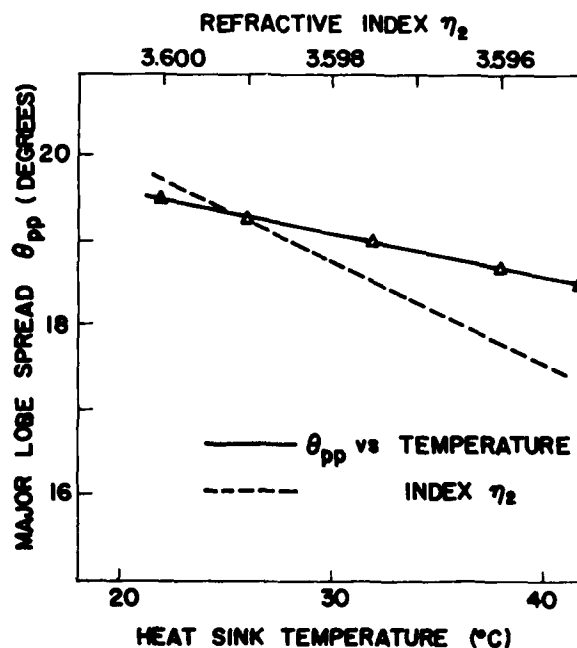FIG. 5. Lasing wavelength vs heat-sink temperature of PL174-1-31.
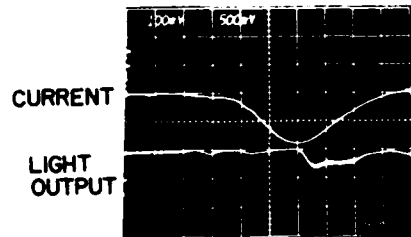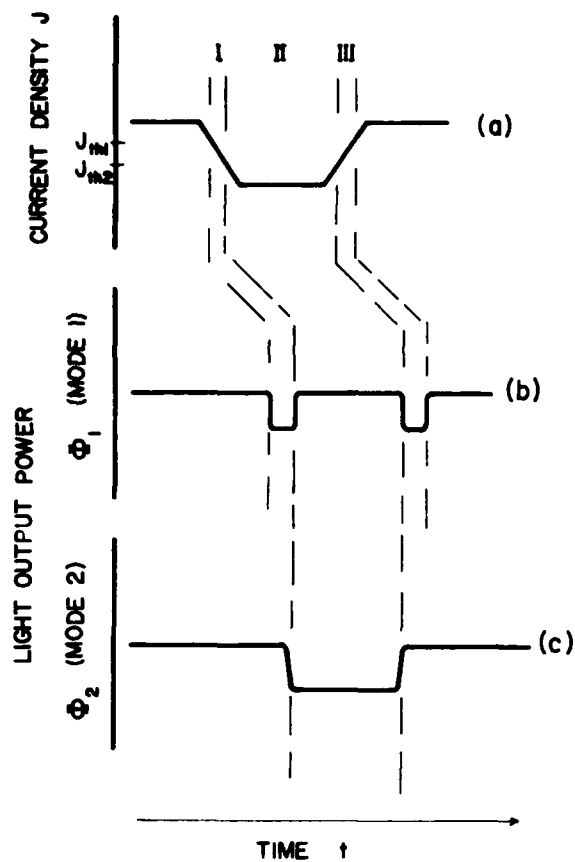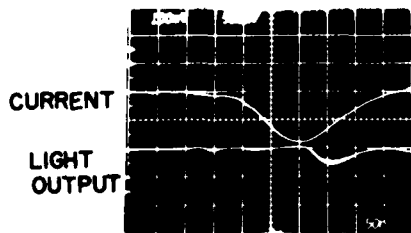

FIG. 7. Experimental θ_{pp} (solid line) vs heat-sink temperature and five-layer waveguide calculated θ_{pp} (dashed line) vs active-region index.

FIG. 8. Time display of input laser current and optical output. In (a) an input current pulse is drawn. J_{th_1} and J_{th_2} are the threshold current densities of the first two modes, respectively. In (b), optical flux Φ_1 at the fundamental mode wavelength is shown to exist in regions I and III. In (c), the second mode optical flux Φ_2 is detected in region II at the second mode wavelength. In (d), the experimental output pulse is shown in the lower trace at the fundamental mode wavelength. The top pulse is the input current. In (e), the lower trace is the second-mode output at its wavelength.

show the cavity selection is sensitive to gain/mode profile coupling and index change with excess carrier injection.

IV. DISCUSSION

The data from Fig. 3 were used with the data from Table I for a multilayer waveguide analysis of the transverse modes. This method was used first to check the accuracy of material parameters. In Fig. 6, the dashed line shows a close fit with the solid measured curve of the far field. The pip on one shoulder is a leaky wave coupling to the substrate layer. As previously mentioned, Snell's law dictates a fixed refractive index for the substrate. It was noticed in the experiment that the pip remained stationary in angular displacement with temperature change 20–40 °C and with current drive. Also, the pip remains about 4 dB below the main lobes over temperature and current variations. This means the thickness and refractive index of layer 3 in Fig. 2 should be fixed in order to hold the pip stationary. The only feature to change for the second mode is the angular separation of the major lobes designated as θ_{pp}. These data are represented in Fig. 7 and will be discussed subsequently.

The only way to match the θ_{pp} change with temperature is to slightly decrease the active-layer refractive index with increased current drive. The increase in threshold current of a mode with temperature occurs due to a modal confinement change, internal quantum-efficiency decrease, or a carrier-lifetime or absorption-coefficient change.[20] Near-field measurements did not show a shift of the transverse mode with temperature. The refractive-index change of each layer with temperature $\delta\eta/\delta T$ can be shown to be $1.5 \times 10^{-4}/°K$.[21] For a twenty-degree range, 20–40 °C, $\delta\eta \simeq 0.003$. On the other hand, the index change due to dispersion[21] for a layer is $\delta\eta/\delta E \simeq 0.8/eV$. For $\delta\lambda = 20$ Å from Fig. 5 (the first high-order mode), it can be shown that $\delta\eta \simeq -0.003/\text{Å}$.

The dispersion and heating effects on refractive index of each layer tend to cancel. Therefore, with the evidence that the near field remains constant with temperature, the pip on the shoulder of the far field remains stationary and dispersion and heating effects tend to cancel. it is assumed that the dominant refractive-index change is that of the active layer

TABLE I. Typical values for the physical constants used in the ambipolar diffusion solution.[a]

	Layer 1	Layer 2	Layer 3
Doping	$p\text{-}10^{-18}$	$p\text{-}5 \times 10^{17}$	$n\text{-}5 \times 10^{17}$
Al concentration	20%	0	2%
η	3.48	variable	3.5865
Absorption	5	20.8	2.4
Width	· · ·	2.65×10^{-4}	· · ·
μ_n	3132	3649	3649
μ_p	138	167	167
D_n	81.0	198	128
D_p	3.67	4.65	4.33
τ	7.69×10^{-9}	3.59×10^{-9}	8.46×10^{-9}
D^*	80.6	15.6	6.8
L^*	7.87×10^{-4}	2.37×10^{-4}	2.4×10^{-4}

[a] All quantities are in cgs units, with the exception of mobility which is in the mixed units cm²/V sec and absorption which is in cm⁻¹.

TABLE II. Calculated values for threshold current density, modal absorption and internal differential quantum efficiency obtained from the ambipolar diffusion solution.

	Mode 1	Mode 2
Threshold current density (kA/cm²)	15.58	16.93
Modal absorption (cm⁻¹)	19.74	6.38
Internal differential quantum efficiency (%)	66.8	72.8

due to injection level. The data of Tables I and II and Fig. 3 are used to find the solution to the ambipolar diffusion equation. A rise in temperature is represented by a reduction in refractive index as required in matching the far-field pattern of Fig. 6.

With the relevant material parameters listed in Fig. 3, a solution was found for the ambipolar diffusion equation. In Fig. 9 the threshold current density for the first two modes is plotted as a function of the active-region refractive index. For larger η_2 values (corresponding to a larger index step) the second mode has the lowest threshold due to superior coupling to the excess carrier distribution. But as the active-region index is lowered and the second mode approaches cutoff, its coupling efficiency diminishes and the fundamental mode emerges with the lowest threshold.

Typical material parameters calculated (fundamental mode at $\eta_2 = 3.5948$) are shown in Table I. Since many of the parameters depend on injection levels, the quantities in Table I vary slightly over the graphs presented. With these calculated values, the usefulness of the ambipolar equation can be shown for the active layer. The calculated hole-injection efficiency is 99.4% and the electron-injection efficiency is 86% for this case. This calculation predicts a crossover point at a slightly lower η_2 value than the multilayer mode range in Fig. 7. This is because in the multilayer model, the presence of the substrate with a relatively high refractive index increases the active-region eigenvalue. For instance, if the buffer-layer thickness d_1 were decreased, the active–layer eigenvalue would shift even more.

Figure 9 is useful in interpreting the phenomena shown in Fig. 4. The fundamental mode does not occur below 30 °C. At 20 °C, the second mode has a threshold current density of about 12 kA/cm². However, abruptly above 30 °C, the fundamental mode appears. From Fig. 8, a slight change in η_2 on the order of $\delta\eta_2 = -0.002$ is sufficient to cause a crossover in threshold currents between the two modes. Both Figs. 4 and 9 show that the second-mode threshold increases sharply after the crossover. Threshold current densities predicted by the ambipolar solution are in fair agreement with experimental values.

Modal output power as a function of current density is plotted in Fig. 10. Because the linear theory of gain is assumed, only one mode at a time is calculated. At power levels above threshold, the modal gain is assumed pinned at its threshold value. Note that the second mode, despite higher threshold current density and reduced coupling efficiency, has a higher internal differential quantum efficiency than the fundamental mode. Thus, for a sufficient overdrive beyond threshold, the second mode will eventually be the more efficient overall and will dominate. An explanation for this higher internal differential quantum efficiency can be seen in Table II. The modal absorption of the second mode is low because a significant portion of its energy is propagating outside the lossy active region whereas most of the fundamental mode is well confined to the active region. Since modal loss dominates slope efficiency, the second mode has the higher value. This higher value, in conjunction with a higher threshold due to poorer coupling efficiency, causes the mode efficiency crossover point.

With these results, the phenomena of mode crossover in this laser can be understood. At 20 °C the second mode has the lower threshold and higher efficiency and consequently only the second mode appears. At an intermediate temperature, the second mode will appear at high-enough current overdrive due to better slope efficiency. Above 42 °C, the threshold for the second mode becomes prohibitive. Figure 8 depicts a time resolution between the two modes at an intermediate temperature. Figure 8(a) represents an input drive pulse. The two threshold current densities for the two modes are labeled J_1 and J_2. As the current pulse rises above J_1 the first mode turns on in region I. Output flux Φ_1 for the first mode is represented in Fig. 8(b). As the input current progresses to J_2, region II is entered. The second mode turns on, as shown in Fig. 8(c), as Φ_2. Finally, with the drop of input current, region III is entered and first mode reappears. As shown in Figs. 8(d) and 8(e), this situation is observed experimentally. In Fig. 8(d), the monochromator is set on the first-mode wavelength and the lower pulse is the output power. Reviewing the two output pulses, it can be seen the two modes have a time separation during a current pulse. This is explained by the fact that, from Fig. 9, the second-mode threshold can still be reached slightly after crossover. From Fig. 10, the second mode clearly is predicted to dominate the first mode if threshold can be reached, due to better efficiency.

Theoretical mode and excess carrier coupling for the laser is shown in Fig. 11, where the excess carrier profile is plotted across the active layer for the two modes operating at
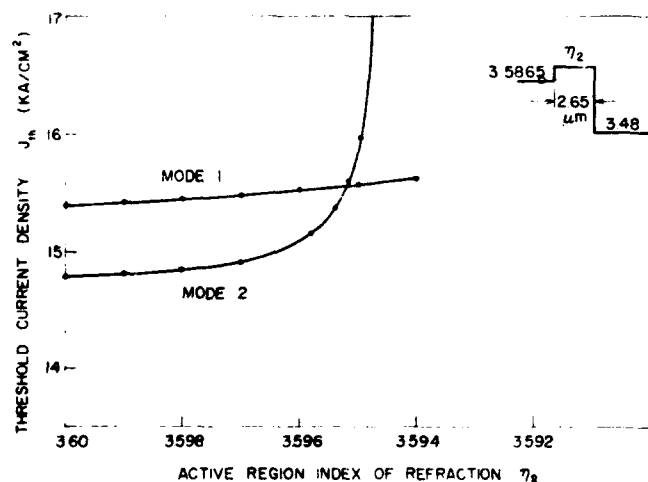

FIG. 9. Ambipolar diffusion solution. Threshold current density for the first-and second-order modes is plotted against the active-region index η_2.
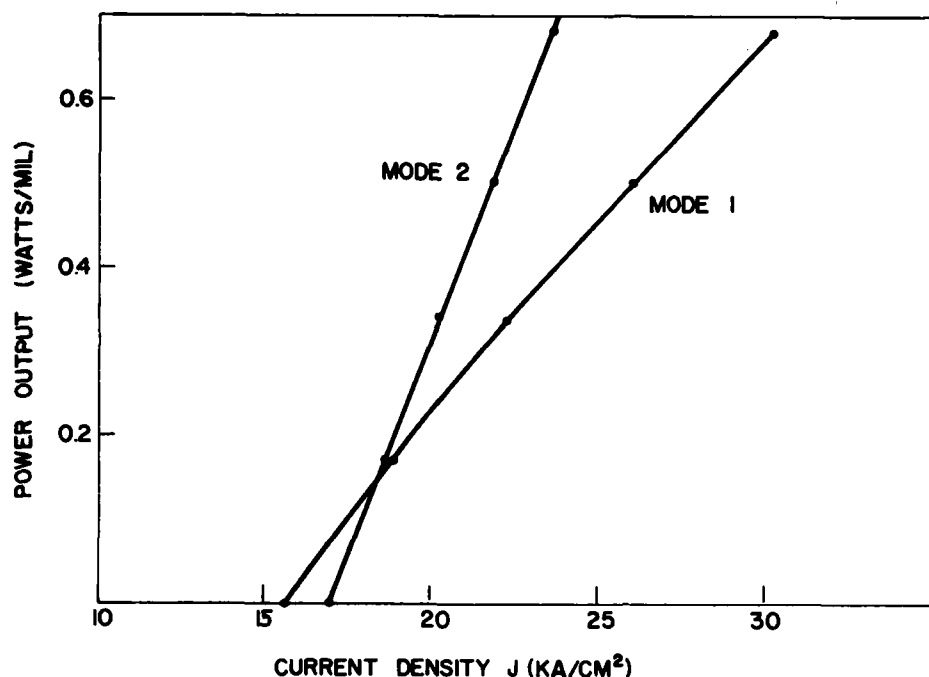
FIG. 10. Ambipolar diffusion solution. Output power is plotted against threshold current density for the first two modes. The slight curvature in the mode 1 curve is caused by carrier redistribution. The index $\eta_2 = 3.5948$.

two power-output levels (threshold and 0.67 w/mil.). Included on the carrier plot is the normalized modal distribution. Several factors should be noted. First, the second-mode distribution is clearly penetrating the passive n layer, indicating a near cutoff situation and a modal loss dominated by the n-layer absorption. With all curves normalizd, a simple product of δp and E^2, integrated over the active region, shows the fundamental mode better coupled than the second, as expected. Second, it can be seen that the carrier profile peaks on the side where holes are injected. This profile contradicts the notion that electron injection dominates and the peak occurs on the n side. Since the charge cloud is ambipolar, it must accommodate the low-hole mobility to maintain quasi-charge neutrality. Hence, the profile is skewed toward the hole injection or p side of the active layer. As expected, carrier profiles change shape with current density.

As a final note, we use the refractive-index dependency of the active region on temperature and hence current density to estimate the free-carrier effect. The influence of free carriers on the refractive index in a material is determined from the classical theory of dispersion. The refractive index in the presence of free carriers η is related to the refractive index in the absence of carriers $\bar{\eta}$ by

$$\eta^2 = \bar{\eta}^2 \left(1 - \frac{4\pi N q^2}{m^* \omega^2 \bar{\eta}^2} \right). \tag{15}$$

Here, m^* is the effective mass of the carrier, q is the charge of an electron, N is the carrier density, $\omega = 2\pi c/\lambda$, and ϵ_0 is the vacuum permittivity. Since the change in index is much smaller than $\bar{\eta}$, Eq. (15) can be rearranged to

$$\delta\eta_{fc} \simeq \frac{2\pi N q^2}{m^* \omega^2 \bar{\eta}}. \tag{16}$$

In other words, the change in index due to free carriers is directly proportional to the concentration of free carriers

$$\delta\eta_{fc} = K N, \tag{17}$$

where K is a constant we wish to determine. By plotting refractive-index change versus carrier increase, the constant K would be the slope at a particular point

$$d(\delta\eta_{fc}) = K d(N) \tag{18}$$

or

$$K = \frac{d(\delta\eta_{fc})}{d(N)}. \tag{19}$$

A change in a particular parameter, say lifetime τ, with injection would be reflected in Eq. (17) having a nonzero second derivative. We take $\delta\eta_{fc}$ from Fig. 7 and conclude that this index change is very nearly a linear function of temperature. However, we find from Fig. 4, carrier concentration N, related to the peak threshold current, is not quite a linear function with temperature. Therefore, under the assumption the free-carrier effect is the dominant cause of observed pattern change , the constant K would be precisely

$$K = \frac{d(\delta\eta_{fc})/dT}{d(N)/dT}.$$

This expression contains the information that K is not a true "constant" but is itself a slight function of injection level. Nevertheless, it is instructive to estimate K using Eq. (19) to compare with conventional theory. Using

$$N = \frac{J\tau}{q d_2}$$

and a straight line approximation to $d(N)$ over the temperature range 20–42 °C we get

$$K = -3.1 \times 10^{-21} \text{ cm}^3, \quad \tau = 3 \text{ nsec}$$

and

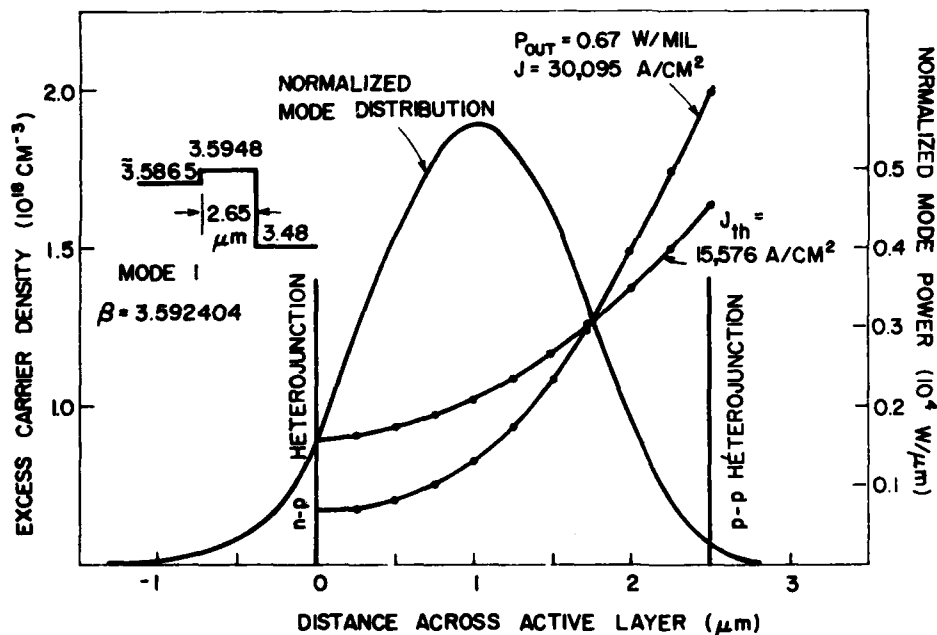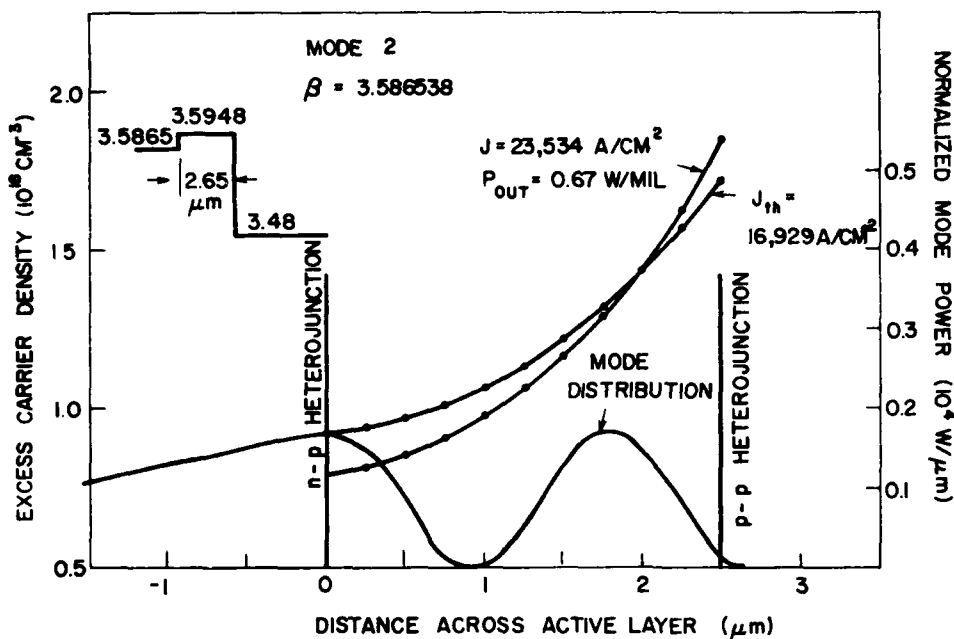$$K = -6.2 \times 10^{-21} \text{ cm}^3, \quad \tau = 2 \text{ nsec}.$$

FIG. 11. Excess carrier densities plotted across the active region for the ambipolar diffusion equation. In (a), the second-mode distribution is plotted. In (b), the first-mode distribution is shown. Note in (a) that the second mode "tail" extends into the n cladding.

These results can be compared to $K = -4 \times 10^{-21}$ cm^3 from Thompson[22] and $K = -(5-11) \times 10^{-21}$ cm^3 from Selway.[23] Thompson used $\tau = 3$ nsec for his calculation. Several other values for K have recently been reported. Olsson and Tang[24] report $K = -(4.9 \pm 0.4) \times 10^{-21}$ for $\tau = 2.2$ nsec. Henry et al.[25] report $K = -(1.8 \pm 0.4) \times 10^{-21}$ for lasers with carrier densities estimated at 1.02×10^{18} cm^{-3}.

V. CONCLUSION

A solution for the ambipolar diffusion was presented for the active region of a double heterojunction laser. Along with the solution of modes from Maxwell's equations in a multilayer waveguide, this combined description was applied to a broad-area heterojunction laser. The refractive-index change of the active region with temperature was estimated from far-field pattern matching of the transverse modes. Transverse-mode-selection conditions were predicted with the diffusion equation and compared with the transverse-mode selection of the sample laser.

Mode threshold was shown to depend on coupling efficiency between excess carriers and modal distribution in the active layer. The differential internal quantum efficiency depends primarily on mode absorption and injection efficiency. Mode crossover occurs when the mode with the highest threshold also has the highest slope efficiency.

Carrier transport in a semiconductor laser is an ambipolar diffusion process which can be described using the relaxation time approximation. In bulk regions, quasi-charge

neutrality is satisfied because of the strong internal field between electrons and holes. The active region of a semiconductor laser undergoes double injection: hole injection from the p side and electron injection from the n side. In devices with good injection efficiencies, the injected carrier profile is higher at the p-p, rather than at the p-n, interface because of low hole mobility.

The device modeled here shows a distinct peak of carriers on the p-p interface. The slope of the carrier profile increases with increased current density. Since these carrier profiles demonstrate significant skewing, it is clear that this can affect mode selection if the modal shape couples poorly with the carrier concentration.

ACKNOWLEDGMENTS

[1] J. C. Dyment, Appl. Phys. Lett. **10**, 84 (1967).

[2] J. E. Ripper, J. C. Dyment, L. A. D'Asaro, and T. L. Paoli. Appl. Phys. Lett. **18**, 155 (1971).

[3] J. C. Dyment, L. A. D'Asaro, J. C. North, B. I. Miller, and J. C. Ripper, Proc. IEEE **60**, 726 (1976).

[4] R. D. Burnham and D. R. Scifres, Appl. Phys. Lett. **27**, 510 (1975).

[5] D. Botez, W. Tsang, and S. Wang, Appl. Phys. Lett. **28**, 234 (1976).

[6] P. A. Kirkby and G. H. B. Thompson, J. Appl. Phys. **47**, 4578 (1976).

[7] K. Aiki, M. Nakamura, T. Karoda, J. Omeda, R. Ito, N. Chinone, and M. Maeda, IEEE J. Quantum Electron. **QE-14**, 89 (1978).

[8] J. P. McKelvey, *Solid State and Semiconductor Physics* (Harper & Row, New York, 1966).

[9] W. Van Roosbroeck, Phys. Rev **91**, 282 (1953).

[10] B. W. Hakki, J. Appl. Phys. **45**, 288 (1974).

[11] F. Stern, IEEE J. Quantum Electron. **QE-9**, 290 (1973).

[12] G. W. 'tHooft, Appl. Phys. Lett. **39**, 389 (1981).

[13] J. K. Butler, J. Appl. Phys. **42**, 4447 (1971).

[14] M. Cross, IEEE J. Quantum Electron. **QE-9**, 517 (1973).

[15] R. R. Shurtz, *Mode and Recombination Control in Semiconductor Lasers*, Ph.D. Dissertation, University Microfilms International, No. 76-3782, (1975).

[16] E. Pinkas, B. I. Hayashi, and P. W. Foy, J. Appl. Phys. **43**, 2877 (1972).

[17] J. C. Dyment, F. R. Nash, C. J. Hwang, C. A Rozonyi, R. C. Hartman, H. M. Marcos, and S. F. Haszky, Appl. Phys. Lett. **24**, 481 (1974).

[18] H. Kressel, H. F. Lockwood, and J. K. Butler, J. Appl. Phys. **44**, 4095 (1973).

[19] H. C. Casey, Jr., D. D. Sell, and M. B. Panish, Appl. Phys. Lett. **24**, 63 (1974).

[20] H. Kressel and J. K. Butler, *Semiconductor Lasers and Heterojunction LED's*, (Academic, New York, 1977).

[21] F. Stern, Phys. Rev. **133**, A1653 (1964).

[22] G. H. B. Thompson, Opto-Electron. **4**, (1972).

[23] P. R. Selway, G. H. B. Thompson, G. D. Henshall, and J. E. A. Whiteway. Electron. Lett. **10**, 453 (1974).

[24] A. Olsson and C. L. Tang, Appl. Phys. Lett. **39**, 24 (1981).

[25] C. J. Henry, R. A. Logan, and K. A. Bertness, J. Appl. Phys. **52**, 4457 (1981).